Mechanical Characterization of Plastic Ball Grid Array Package Flexure Using Moiré Interferometry

Eugene A. Stout, Nancy R. Sottos, and Andrew F. Skipor

Abstract—**Most previous studies of PBGA packaging reliability focus on the effect of thermal cycling. However, as portable electronic products such as cellular phones and laptop computers are reduced in size and become more readily available, isothermal flexural fatigue also becomes an important reliability issue. Solder interconnects subjected to mechanically induced deformation may result in failure. In the current work, Moiré interferometry is used to investigate the influence of PCB flexure on interconnect strains. A versatile testing apparatus is developed to load PBGA packages in four point bending. Moiré fringe patterns are recorded and analyzed at various bending loads to examine the variation in displacement and strain between the components. Solder balls across the entire array experience large shear strains, often resulting in plastic deformation, which reduces service life of the package.**

Index Terms—**Bending, flexure, mechanical reliability, Moiré interferometry, plastic ball grid array (PBGA), solder ball strains.**

I. Introduction

DUE to increased performance of integrated circuits, the evolution of chip carrier design reflects a trend toward smaller size and higher circuit density. High volume assembly techniques require surface mounting of components on printed circuit boards (PCBs). The increased use of chip carriers with many small leads, such as the plastic ball grid array (PBGA) package shown schematically in Fig. 1, has motivated the electronic packaging community to focus attention on reliability of interconnections. Both cyclic thermal and mechanical loading of the package may cause interconnection failure. Variations in strain between the PBGA package components are induced by differences in thermo-mechanical properties of the silicon die, copper lines and glass fiber/epoxy PCBs (see Table I). Understanding the thermal and mechanical response of these various components is critical to improve package design and yield maximum performance and reliability.

Most previous studies of PBGA packaging reliability focus on the effect of thermal cycling. As a result, the techniques to assess and methods to model thermal fatigue and cycling reliability of solder interconnects in electronic packages and area array assemblies such as PBGA packages are widely available in the literature. Examples of recent works include Engelmaier [1], Darveaux *et al.* [2], Skipor *et al.* [3]–[5], Solomon [6], Frear *et al.* [7], Wild [8], and Corbin [9]. One method of assessing thermal fatigue is accelerated thermal testing in which electronic assemblies are cycled through extremes of temperature, typically −40–125°C or 0–100°C. The number of cycles to failure is determined by monitoring interconnect resistance of the assembly. The cyclic fatigue life measured by these tests is useful for comparing package designs, but provides only limited information about the thermomechanical response of individual package components leading to failure. A second method for predicting reliability is the use of finite element analysis which allows for more detailed prediction of stress and strain fields in packaging components and the subsequent interconnect failure under thermal loading. While the finite element method is a useful numerical tool, a precise method of experimental characterization remains essential for understanding the thermomechanical behavior of packaging assemblies. Laser Moiré interferometry has become a widely used technique for accurate measurement of full field thermal deformations and strains due to CTE mismatch in electronic packaging components [10]–[18]. Analysis of Moiré images has quantified the amounts of bending and solder ball shearing due to thermal mismatch, as well as strain concentrations at interconnects where cracks would be likely to initiate.

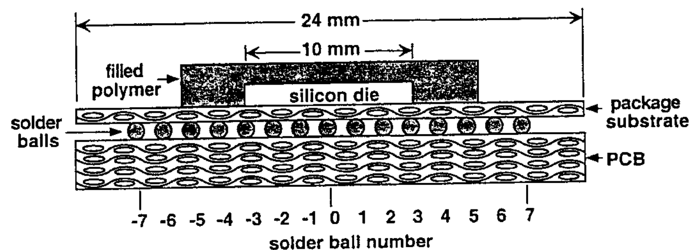

Fig. 1. Dimensioned schematic for a midsectioned 225 I/O PBGA.

TABLE I
ELECTRONIC PACKAGING COMPONENT MATERIAL PROPERTIES AT 23°C

Material	Tensile modulus (GPa)	CTE (ppm/°C)
Silicon [25]	130	2.6
PWB fiberglass [26]	11	12-17 x,y, 63 z
Molding Compound [25]	15.2	15
Copper [25]	121	17
Solder 62% Sn/36% Pb [25]	31.7	21

Manuscript received February 7, 2000; revised May 31, 2000. This work was supported by Motorola Labs, Motorola Advanced Technology Center, Schaumburg, IL.

E. A. Stout is with Motorola, Inc., Northbrook, IL 60062 USA.
N. R. Sottos is with the Department of Theoretical and Applied Mechanics, University of Illinois at Urbana-Champaign, Urbana, IL 61801 USA.
A. F. Skipor is with Motorola Labs, Motorola Advanced Technology Center, Schaumburg, IL 60196 USA.

Publisher Item Identifier S 1521-3323(00)07198-7.

As portable electronic products such as cellular phones and laptop computers are reduced in size, isothermal flexural fatigue also becomes an important reliability issue. Pressing a keypad to actuate a function or type text causes flexure of the package interconnects mounted to the keypad. Although solder interconnects subjected to mechanical cycling fatigue may result in failure, only a few recent studies [19]–[22] address any type of mechanically induced deformation in area array packages. Juso *et al.* [19] conducted bending and drop impact tests on a mounted motherboard. Strain measurements were used to assess mounting reliability. Leicht and Skipor [20] developed a test method to elucidate the mechanical bending fatigue issues in PBGA packages. Specimens consisting of a PBGA component attached to a standard PCB were subject to planar cyclic three point bending. Each solder ball was connected within a series circuit and monitored during loading. Failure was defined as an open circuit within the assembly. While this experiment provided insight to when and where connections failed during bending fatigue, it did not yield any specific information about stress and strain fields in the individual solder balls. More detailed Moiré measurements were carried out by Wang *et al.* [22], but the focus was on interfacial fracture of a flip-chip package due to a concentrated line load.

The current investigation adopts the Moiré technique to quantify the influence of PCB flexure on interconnect strains. A versatile testing apparatus is developed to test PBGA packages in four point bending. Moiré fringe patterns are recorded and analyzed at various bending loads to examine the variation in displacement and strain between the components.

II. Experimental Procedure

A. Experimental Apparatus

A micromechanical test apparatus was developed for use in conjunction with a compact four beam Moiré interferometer (PEMI model 2001-X, IBM Corp.) to test PBGAs and other small electronic components in bending. All of the optics for the four-beam interferometer are enclosed in a single cabinet with only necessary adjustment screws on the outside. Post, Han, and Ifju [23] provide a detailed description of this instrument. The beam from a 632 nm He-Ne laser source enters the cabinet through an optical fiber, passes through several lenses to expand and collimate the beam and is incident upon a 1200 line/mm diffraction grating which divides it into four first order diffracted beams (plus the zero order which is not used). Two of the beams are directed by mirrors on opposite sides of the cabinet to create the U field while the other two beams are reflected by mirrors on the top and bottom of the cabinet to form the V field. A baffle is swiveled back and forth to block the beams of either the U field or the V field. The angle of incidence of the beams onto the sample is 49.4 degrees and the resulting frequency of the virtual grating in the interferometer, f_v, is 2400 lines/mm, twice the sample grating frequency. Light diffracted by the specimen grating is collected by a field lens on the front of the cabinet. Resulting Moiré images are projected in a direction opposite from the loading fixtures and recorded by CCD camera or by Polaroid camera. Test samples are positioned within the 45 mm diameter viewing field of the interferometer using a x-y table, rotation stage, and the screw adjustments on the interferometer. A pneumatic optical table isolates the entire assembly from ambient vibration.

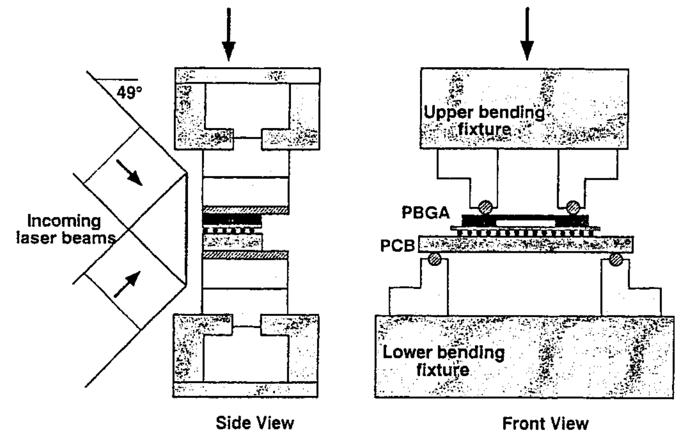

Fig. 2. Schematic of ball grid array sample in four point bending fixtures, front and side view.

The micromechanical tester consists of a rail table driven by a stepper motor (Parker Hannifin Model #506 121S). Stainless steel four point bending fixtures are attached to the rail table through an S-type load cell (Omega Model #LCCA-50). The load cell can withstand a maximum load of 220 N and has a manufacturer's rated accuracy of ±0.08 N. Detailed schematics of the front and side views of the bending fixtures are shown in Fig. 2. Samples are placed at the edge of the fixtures closest to the interferometer so that the incoming laser beams are not blocked. As shown in Fig. 2, the upper fixtures are slotted to permit the motion of the load cell toward the sample center and reduce out of plane bending. The motion of the fixtures and data acquisition from the load cell was controlled using LabVIEW software and a National Instruments Lab NB data acquisition board. Typically, the rail table was moved in specified displacement increments between 30 μm and 100 μm at a velocity of 10 μm/s. Tests were run in which the deflection of the sample was calculated based on the number of steps moved by the stepper motor and the fixture compliance.

B. Sample Preparation

Two different cross-sections were tested to examine the influence of the silicon die on package bending strains. PBGA specimens with 225 IO, 1.5 mm pitch were either sectioned in the middle of the package through the silicon die or near the edge of the package as shown in Fig. 3. To achieve an accurate cut, PBGAs were sectioned using a water cooled low speed diamond wafering blade mounted on a milling machine. This arrangement permitted multiaxis movement of the sample and produced cuts to within 0.1 mm of the midplane of the solder ball row. Despite running the diamond saw blade at speeds as low as 100 rpm, sections through the silicon die often resulted in fracture of the die and some degree of debond from the surrounding mold compound. Grinding the PBGAs with 1500 grit sandpaper left the sample surface free of major flaws produced by cutting. After grinding, specimens were cleaned using a three step process of washing with distilled water, cleaning with water

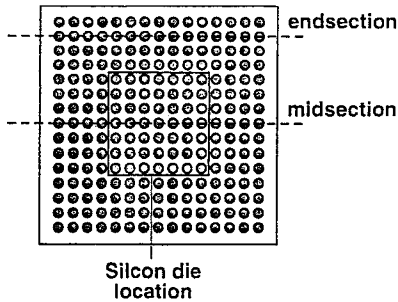

Fig. 3. Location of of PBGA cross sections (die shown in center).

in an ultrasonic cleaner for two minutes, and rinsing with alcohol. This treatment insured that loose debris would not contaminate the cloth disks used in polishing or create flaws in the diffraction grating. Polishing using a 6 μm diamond paste with a water based lubricant removed most remaining surface flaws. After polishing, the same surface cleansing procedure was repeated to remove any remaining debris in preparation for grating application.

Diffraction gratings were applied to the samples using a technique similar to that described by Post, Han, and Ifju [23]. First, a submaster of a 1200 line/mm cross-lined master grating was replicated using GE RTV 615 silicon rubber. The silicon rubber was degassed in a vacuum jar for approximately ten minutes until all visible air bubbles had collapsed. A 3 cm diameter pool of the degassed silicon rubber was then poured on a clean and primed glass plate. The master grating was pressed onto the silicon rubber for replication. After allowing the RTV 615 to cure for 24 hours, the master and submaster were separated using a specially designed fixture which permitted the controlled separation of the gratings while minimizing the bending loads on the glass plates.

A low viscosity epoxy (Tra-Con F114) was carefully applied to the polished surface of the PBGA package and the samples were then applied directly to silicone rubber submasters. The PBGA samples were then separated from the submaster after the epoxy had cured and were subsequently coated with aluminum in a vacuum evaporator. The orientation of the grating lines required that the perimeter of the specimens be square with respect to the edges of the grating. In this way, Moiré fringes corresponded to displacements along the major and minor axes of the specimen.

C. Moiré Image Recording and Analysis

Fringe patterns from the compact interferometer were recorded directly with a large format polaroid camera or with a CCD camera. These images were either stored as TIFF files directly from the CCD camera or as TIFF files digitally scanned from type 52 or 57 Polaroid Land film. To determine the sign of fringe gradients experimentally, fixtures were translated in the positive x or y directions by manually applying pressure to fixtures. The direction of fringe motion was recorded for all solder ball images.

The relation between fringe order and displacement in the x and y directions is expressed as [23]:

$$U = \frac{1}{f_\nu} N_x \tag{1}$$

$$V = \frac{1}{f_\nu} N_y \tag{2}$$

where f_ν is the virtual grating frequency, N_x is the fringe order in the U-field, and N_y denotes the fringe order in the V-field. Strains are calculated from the Moiré fringes by approximating the partial derivatives of displacement by the ratio of the number of fringes along a line to the length of that line:

$$\varepsilon_{xx} = \frac{\partial U}{\partial x} \approx \frac{1}{f_\nu} \frac{\Delta N_x}{\Delta x} \tag{3}$$

$$\varepsilon_{yy} = \frac{\partial V}{\partial y} \approx \frac{1}{f_\nu} \frac{\Delta N_y}{\Delta y} \tag{4}$$

$$\gamma_{xy} = \frac{\partial V}{\partial x} + \frac{\partial U}{\partial y} \approx \frac{1}{f_\nu} \left(\frac{\Delta N_y}{\Delta x} + \frac{\Delta N_x}{\Delta y} \right) \tag{5}$$

To obtain fringe counts along gage lengths, Moiré fringe patterns were analyzed using the image processing software package NIH Image®. The fringe count ΔN across a gage length was measured by positioning an intensity measuring tool within a digitized Moiré image. As a result of mechanical preloading or replicated grating imperfections, initial U and V fields were always populated with at least one fringe. These initially populated fields were analyzed in order to provide initial values for strain and displacement. Therefore, all strains were calculated by subtracting an initial field from a final field to obtain the change in strain or displacement across a gage length. Consequently, a single strain measurement required fringe counts from two different Moiré images such that

$$\Delta N_i = N_{2i} - N_{1i} \tag{6}$$

where $i = x$ or y. Depending upon the quality of the sample and the fringe contrast of the image, fringe orders could be counted to within a quarter to an eighth of a fringe.

The reliability of the experimental method and testing apparatus was established through four point bending experiments on aluminum bars with known material properties. The strains and displacements measured using the Moiré interferometer were found to be in good agreement with values predicted using beam theory. Details of the experiment and comparison of theory and experiment are described in the Appendix . Estimates of the experimental error are also calculated in the Appendix.

III. Flexural Testing of PBGAS

To investigate the response of PBGAs to mechanically induced flexure, midsectioned and endsectioned PBGA samples were placed in four point bending as shown in Fig. 2. All bending tests were performed with the upper bending fixtures placed on top of the chip carriers such that loading pins were situated between solder ball numbers −6 and −5, and 5 and 6 (see Fig. 1). Three midsectioned and three endsectioned PBGA samples were tested under applied loads ranging from 0 to 190

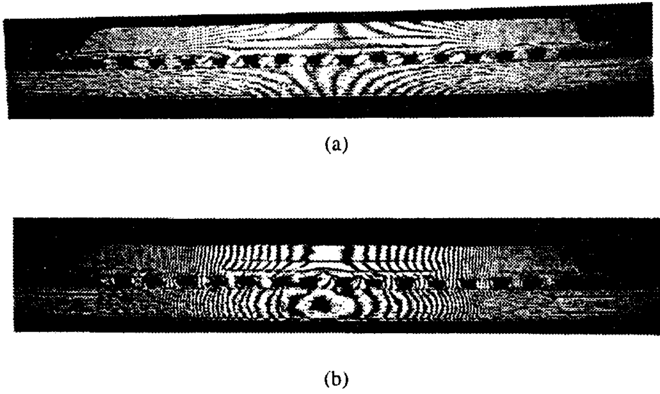

(a)

(b)

Fig. 4. Moiré fringes of a midsectioned PBGA package in four point bending at 0.32 Nm: (a) U field, (b) V field.

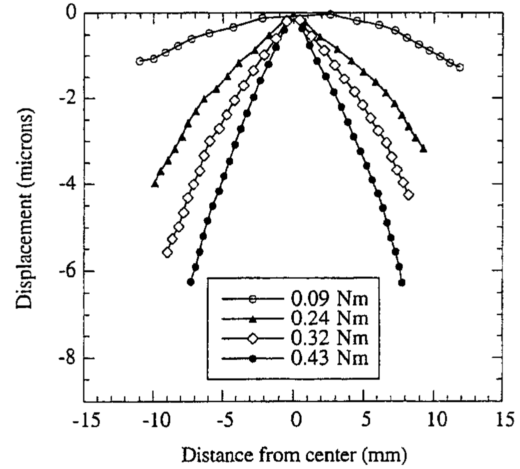

Fig. 5. Bending displacement along the top of the molding compound in a midsectioned PBGA.

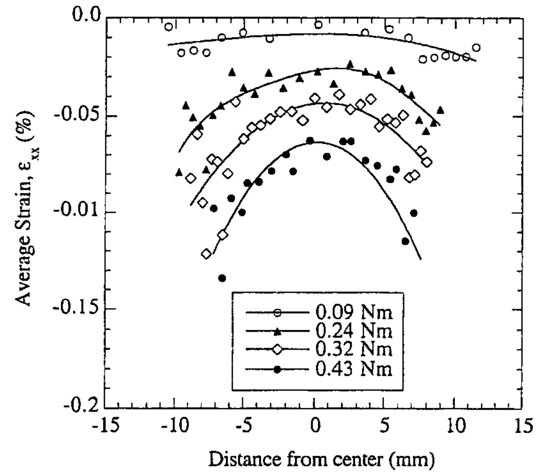

Fig. 6. Bending strain along the top of the molding compound in a midsectioned PBGA.

N. The resulting bending moment in the center section of the sample was calculated as

$$M_m = \frac{(P - P_i)L}{2} \tag{7}$$

where M_m is the change in applied moment, P is the total applied load, P_i is the load at which the initial U and V field were recorded, and L is the moment arm. The change in applied moment M_m corresponds to the change in deformation recorded by the compact Moiré interferometer used in four point bend testing.

A. Midsectioned PBGAs

Typical U and V field Moiré images for a midsectioned PBGA subject to a bending moment of 0.32 Nm are shown in Fig. 4. The applied bending moment results in tensile strains in the lower region of the PCB and compressive strains in the upper region of the molding compound. The hyperbolic pattern of the U field and elliptic pattern in the V field of both these regions are similar to the U and V fields of a rectangular bar in bending (see Fig. 16). However, the presence of the silicon die causes a noticeable variation in the fringe gradient $\partial N_x/\partial x$ along the top of the molding compound. In Fig. 4(b) the variation of the fringe gradient $\partial N_y/\partial x$ along the top of the molding compound indicates a sharp change in the curvature of the upper PBGA surface. In contrast to an isotropic bending sample, Moiré images of the PBGA sample do not have a clearly defined neutral axis in the center of the sample. Along the lower edge of the chip carrier, ε_{xx} changes from almost zero near the silicon wafer to tensile on either side of the die. The fringe gradient $\partial N_x/\partial x$ also changes along the top of the PCB from positive near the silicon die to negative on either side of the wafer. These changes in fringe gradient indicate that ε_{xx} varies such that the chip carrier is not entirely in compression and that the PCB is not purely in tension.

1) Mold Compound and PCB Strains: The displacements and strains in the x direction were calculated at points along the top of the PBGA mold compound and along the bottom of the PCB. Displacements along the top of the molding compound are plotted in Fig. 5 for bending moments ranging from 0.09 Nm to 0.43 Nm. The corresponding strain data in Fig. 6 reveals the variation in ε_{xx} along the top of the molding compound near the silicon die. The silicon die extends from -5 mm to 5 mm in both Figs. 5 and 6 underneath the surface of the molding compound. The compressive strain in the molding compound was a minimum in the center of the sample and increased sharply near the edge of the wafer. The displacements and strains along the bottom of the PCB are plotted in Figs. 7 and 8, respectively. The strain ε_{xx} was tensile and similar in magnitude to the top of the board. The fringe density was so high in the regions outside of -10 mm to 10 mm that an accurate determination of fringe location could not be made. This high fringe density also indicated a trend of greatly increasing strain on either side of the region near the silicon die.

2) Solder Ball Strains: Bending tests were performed on two different samples to characterize the deformation of solder ball joints. Moiré images of individual solder joints were recorded over a range of loads. Average strains ε_{xx}, ε_{yy}, and γ_{xy} were calculated using (3)–(5) and plotted in Figs. 9–11. The dashed lines in the graphs denote the locations of upper bending fixture loading points with respect to the horizontal locations of solder balls. The normal strains ε_{xx} and ε_{yy} plotted in Figs. 9 and 10 are nearly zero in the center of the solder ball array. However, solder balls near the application of loading

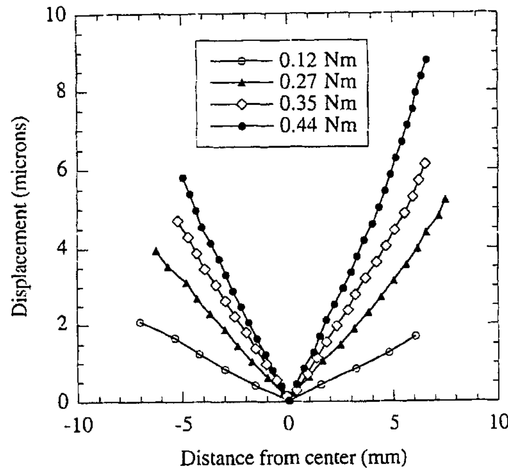

Fig. 7. Bending displacement along the bottom of the PCB in a midsectioned PBGA.

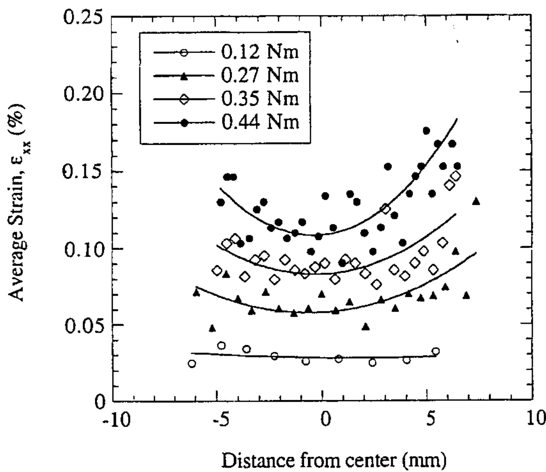

Fig. 8. Bending strain along the bottom of the PCB in a midsectioned PBGA.

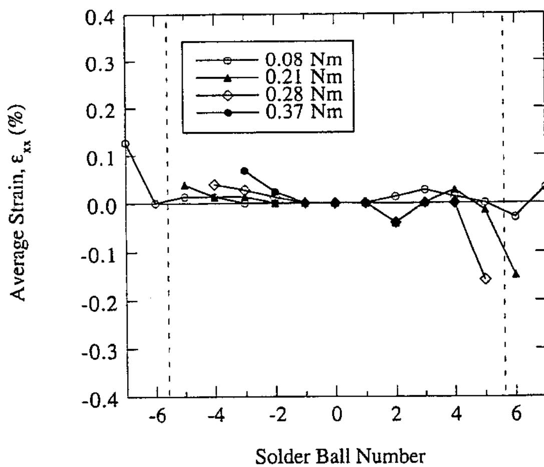

Fig. 9. Average strain ε_{xx} for midsectioned PBGA solder balls under bending.

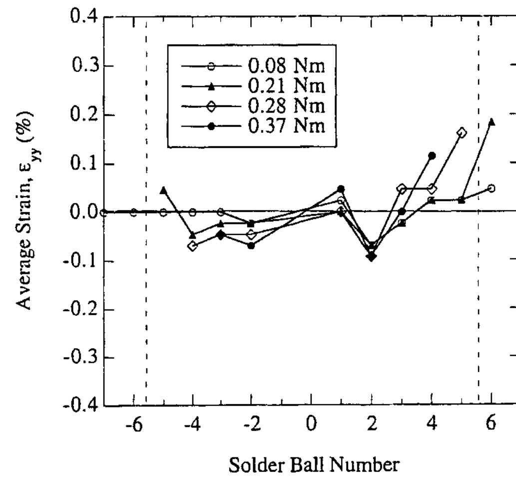

Fig. 10. Average strain ε_{yy} for midsectioned PBGA solder balls under bending.

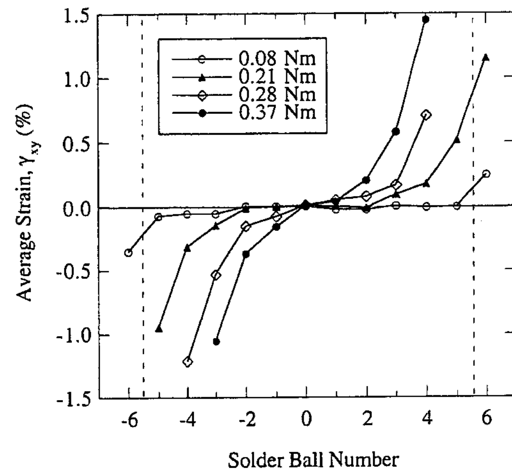

Fig. 11. Average strain γ_{xy} for midsectioned PBGA solder balls under bending.

points experience strains of measurable magnitude. Using the method presented in the Appendix , the uncertainties in ε_{xx} and ε_{yy} are estimated as ± 0.0002 and ± 0.0003, respectively for the maximum value of applied moment. Average strain values were not calculated for all solder balls at high loads because the solder ball fringe pattern densities were noticeably inhomogeneous. One possible reason the normal strains are nearly zero except in regions near the loading points may be the method of loading itself. Moving the loading points to the PCB from the package could improve results.

Maximum average solder ball shear strains plotted in Fig. 11 were nearly an order of magnitude higher than maximum average normal strains for the mid-sectioned samples. The uncertainty for γ_{xy} was calculated to be ± 0.0008. All but the center solder ball experienced significant shear strain due to bending. At relatively high bending loads, outlying solder balls tended to deform plastically. This deformation produced inhomogeneous fringe patterns. Fig. 12 shows the progression of fringe patterns with increasing applied bending load in solder ball #5 of the sample. The presence of the copper pads connecting the solder ball to the chip carrier and PCB is marked by the sharp discontinuities in the V field fringe patterns of Fig. 12. After unloading the sample, the complicated fringe patterns remained on the outermost solder balls. This remaining complex fringe pattern indicated that the bending load had induced plastic deformation in

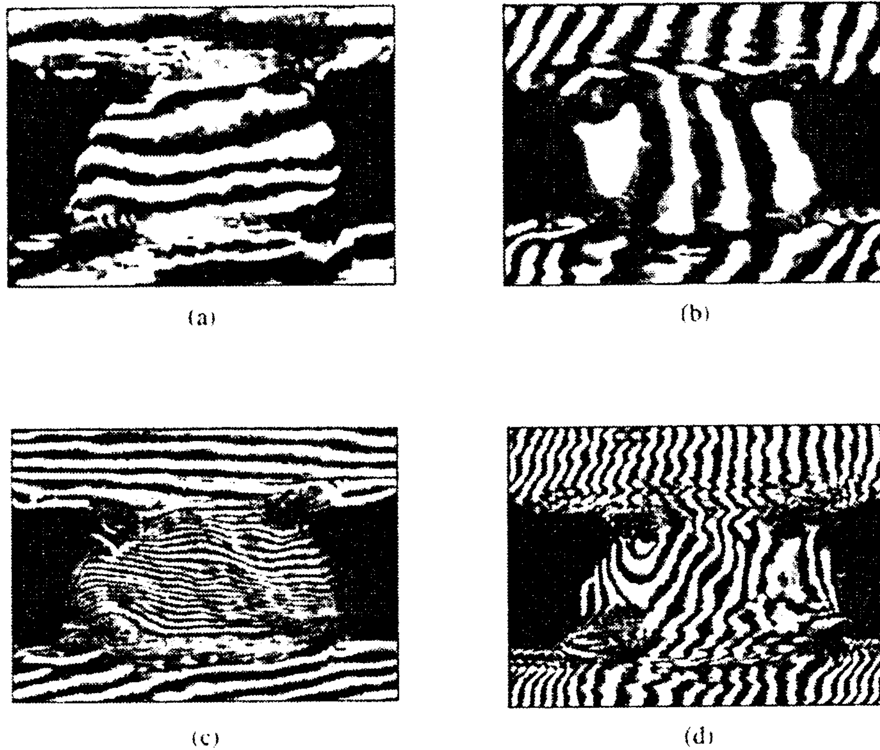

Fig. 12. Bending induced deformation of midsectioned sample solder ball #5): (a) U field at 0.26 Nm, (b) V field at 0.26 Nm, (c) U field at 0.44 Nm, (d) V field at 0.44 Nm.

the solder joints. Although γ_{xy} varies across the solder ball, the shear strain terms are dominated by $\partial N_x/\partial y$. The dominance of $\partial N_x/\partial y$ over $\partial N_y/\partial x$ is made clear by comparing Fig. 12(a), (b). Since $\partial N_x/\partial y$ is significantly higher than $\partial N_y/\partial x$, the outer solder balls are nearly in a state of simple shear.

B. Endsectioned PBGAs

To determine whether the presence of the silicon die had a significant influence on the distribution of bending induced displacements, endsectioned PBGAs were also tested. Representative Moiré fringe patterns for an endsectioned PBGA are shown in Fig. 13 for an applied bending moment of 0.33 Nm. The overall distribution of the fringe patterns for the U field images are more similar to the isotropic bar in bending than the midsectioned samples. This increased continuity of fringe patterns results from the absence of the silicon die along the cross section. Consequently, the distribution of the displacements and strains along the top of the molding compound plotted in Figs. 14 and 15 for a range of applied bending moments are more uniform than those for the midsectioned PBGAs. Like midsectioned samples, the fringe gradient $\partial N_x/\partial x$ /rises outside the region $(-10$ mm to 10 mm) such that accurate displacement measurements could not be made. The displacements and strains along the bottom of the PCB (not shown) have shapes similar to those of midsectioned sample displacements and strains in Figs. 7 and 8. This similarity indicates that strain along the bottom of the PCB is not significantly influenced by proximity to the silicon die.

Endsectioned solder balls deformed in a manner similar to solder balls in midsectioned samples. The distribution of average strains calculated for the endsectioned samples (not shown) followed the same general trends as plotted for the midsectioned samples in -11. Maximum strains occurred in the outer most rows of solder balls and plastic deformation was observed at high bending loads. Thus, the selection of cross section had no noticeable influence on the distribution of solder ball average strains.

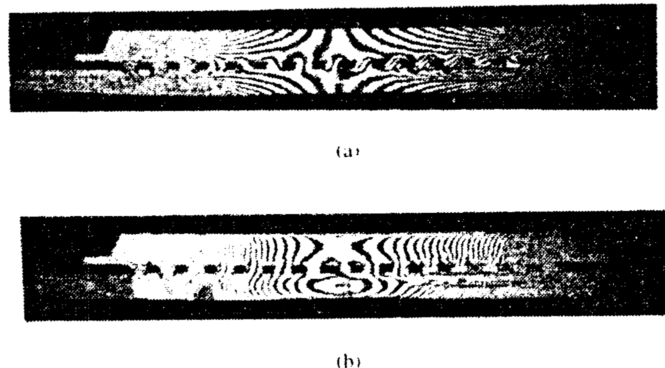

Fig. 13. Moiré fringes for an endsectioned PBGA package in four point bending at 0.326 Nm: (a) U field, (b) V field.

IV. Conclusions

A micromechanical test apparatus was developed to load electronic packages in four point bending. The resulting displacement and strain fields were measured with a compact Moiré interferometer and provide a detailed examination of area array electronic packaging response to flexure. The reliability of the experimental apparatus and method was verified

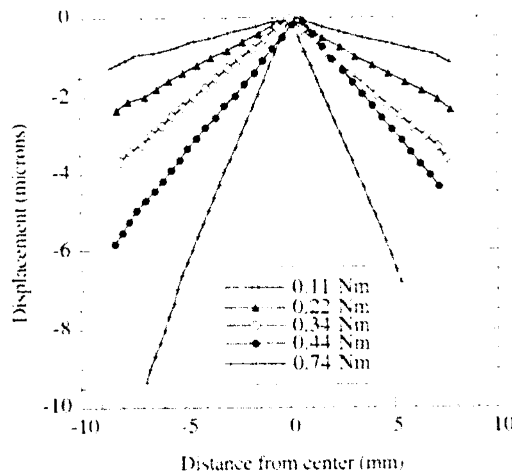

Fig. 14. Bending displacement along the top of the molding compound in an endsectioned PBGA.

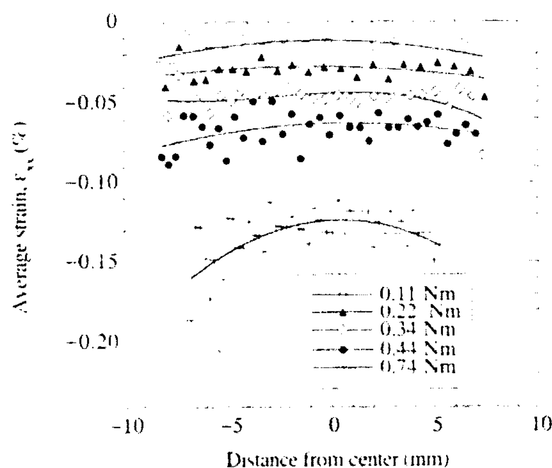

Fig. 15. Bending strain along the top of the molding compound in an endsectioned PBGA.

by testing a standard aluminum bending specimen with known material properties.

Near the region of the solder ball array, displacements due to bending in the PCB and chip carrier were complex. The variation of fringe density around the solder balls revealed the localized influence of solder ball connections on chip carrier and PCB deformation. Very large shear strains developed in solder balls across the entire array. Application of high bending loads resulted in plastic shear deformation of the interconnections. The plastic strain induced by bending could significantly reduce the life of an electronic package subjected to normal thermal cycling. The combined influence of thermal and bending loading on interconnections warrants further investigation.

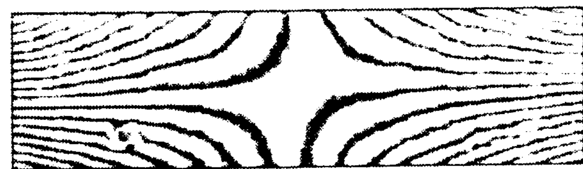

(a)

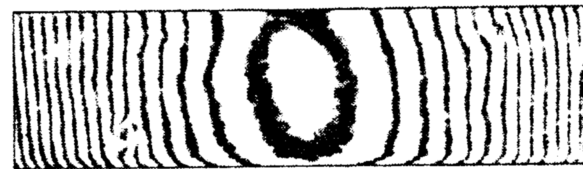

(b)

Fig. 16. Moiré fringes for a rectangular beam in four point bending: (a) U field, (b) V field.

Overall, results indicate that the Moiré technique can be used to identify critical areas of high strain in a PBGA subjected to flexure. In turn, these highly strained areas may be examined and redesigned using computational modeling. By selectively using Moiré data to provide displacement boundary conditions on critical parts of the PBGA assembly, such as solder joints, the need to model an entire PBGA may be eliminated [24]. With a clearer understanding of the connection between sectioned and unsectioned assemblies, the displacement data provided by Moiré interferometry could be used to focus modeling and redesign, as has been done for PBGAs under thermal cycling.

APPENDIX

Diffraction gratings were applied to aluminum bending samples in a fashion similar to that described for the PBGA components in Section II-B. Under a load of 20 N, the bar was aligned with the compact interferometer to produce an initial fringe pattern with a minimum number of fringes for both U and V fields. After photographing both initial fields, the sample was loaded to preset values and photographed again. The Moiré fringes of the loaded bar are shown in Fig. 16. Ideally, a four point bending fixture places the midsection of a sample in pure bending. Elementary beam theory predicts that strain ε_{xx} should be dependent on loading, cross section geometry, and distance perpendicular to the neutral axis of the beam as:

$$\varepsilon_{xx} = -\frac{My}{EI} \tag{8}$$

where M is the applied moment, y is the distance from the neutral axis of the beam, E is the Young's modulus of the material,

$$U_{\varepsilon_{xx}} = \sqrt{\left[\frac{-1}{f_\nu^2}\,\frac{(N_{2x}-N_{1x})}{\Delta x}\,U_{f_\nu}\right]^2 + \left[\frac{1}{f_\nu}\,\frac{1}{\Delta x}\,U_{N_{2x}}\right]^2 + \left[\frac{1}{f_\nu}\,\frac{-1}{\Delta x}\,U_{N_{1x}}\right]^2 + \left[\frac{-1}{f_\nu}\,\frac{(N_{2x}-N_{1x})}{\Delta x^2}\,U_{\Delta x}\right]^2} \tag{9}$$

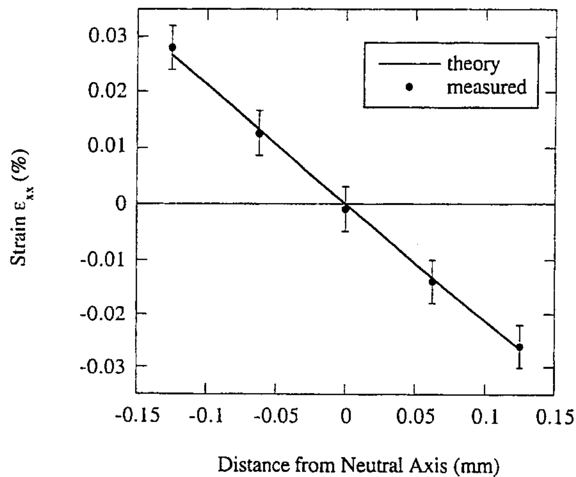

Fig. 17. Predicted strain ε_{xx} for beam in bending and experimental strain calculated from Moiré image.

and I is the moment of inertia of the cross section of the beam. By counting fringes over a gage length between the two inner loading points of both initial and loaded U field photographs, average strain ε_{xx} was calculated and compared with the strains predicted by (8). The strains measured using the Moiré interferometer are compared with values predicted by beam theory in Fig. 17.

Experimental uncertainty in the strain significantly contributes to the scatter in measured values of ε_{xx} shown in Fig. 17. The root mean square uncertainty of strains determined from Moiré images depends upon the measurement of each of the terms in (3)–(5). For example, the root mean uncertainty for the strain in the x direction, $U_{\varepsilon_{xx}}$, is calculated as (9), shown at the bottom of the previous page, where U_{f_v} is the uncertainty in the virtual grating frequency, $U_{N_{2x}}$ is the uncertainty in the change in the loaded U field fringe count, $U_{N_{1x}}$ is the uncertainty in the change of the initial U field fringe count, and $U_{\Delta x}$ is the uncertainty in the gage length. For all Moiré tests U_{f_v} was taken to be 240 lines/mm or 10% of the manufacturers given value for the virtual grating frequency. The measurement of fringe count by the Image® software intensity measurement tool had some uncertainty associated with the tool's alignment or sizing within digitized Moiré fringe patterns. Misalignment or improper sizing of the intensity measurement tool tended to have a larger influence on the uncertainty of the loaded fringe count than on the uncertainty of the fringe count for null fields. For most tests, $U_{N_{1x}}$ was an eighth of a fringe order while $U_{N_{2x}}$ was typically a quarter of a fringe order. The accuracy of the measurement of gage length was also limited by the placement of the Image® software intensity measurement tool to within two or three pixels of a true sample length. For most digitally scanned images, $U_{\Delta x}$ was 0.127 mm. Taking $U_{\Delta x} = 0.127$ mm, $U_{N_{1x}} = 0.125$, $U_{N_{2x}} = 0.25$, and $U_{f_v} = 240$ lines/mm, the average uncertainty calculated for the Moiré bending strain measurements of ε_{xx} was $\pm 0.000\,04$. The term in (9) involving the change in fringe orders, N_{2x} and N_{1x}, dominates the experimental uncertainty for strain. Consequently, the uncertainty involved with the measurement of the change in the number of fringes limits the sensitivity of Moiré based measurements.

References

[1] W. Engelmaier, "Fatigue life of leadless chip carrier solder joints during power cycling," *IEEE Trans Comp., Hybrids, Manufact. Technol.*, vol. CHMT-3, pp. 232–237, Sept. 1983.

[2] R. Darveaux and A. Mawer, "Thermal and power cycling limits of plastic ball grid array (PBGA) assemblies," in *Proc. Surface Mount Int.*, San Jose, CA, 1995, pp. 315–326.

[3] A. F. Skipor, S. V. Harren, and J. Botsis, "On the constitutive response of 63/37 Sn/Pb Eutectic solder," *ASME J. Eng. Mater. Technol.*, vol. 118, pp. 1–11, Jan. 1996.

[4] ——, "The effect of mechanical constraint on the flow and fracture of 63/37 Sn/Pb Eutectic alloy," *Eng. Fracture Mech.*, vol. 52, pp. 647–669, Nov. 1995.

[5] A. F. Skipor and S. V. Harren, "Thermal cycling of temperature and strain rate dependent solder joints," *Mech. Time-Dependent Mater.*, vol. 2, pp. 59–83, 1998.

[6] H. Solomon, "Fatigue of 60/40 solder," *IEEE Trans. Comp., Hybrids, Manufact. Technol.*, vol. CHMT-9, pp. 423–432, 1986.

[7] D. Frear, D. Grivas, and J. W. Morris, Jr., "A microstructural study of the thermal fatigue failures of 60Sn-40Pb solder joints," *J. Electron. Mater.*, vol. 17, pp. 1710–1718, 1988.

[8] R. Wild, "Some fatigue properties of solders and solder joints," *InterNepcon*, Oct. 1975.

[9] J. S. Corbin, "Finite element analysis for solder ball connect (SBC) structural design optimization," *IBM J. Res. Develop*, vol. 37, no. 5, pp. 585–596, 1993.

[10] A. F. Bastawros and A. S. Voloshin, "Thermal strain measurements in electronic packages through fractional fringe Moiré interferometry," *ASME J. Electron. Packag.*, vol. 112, pp. 303–308, 1990.

[11] B. T. Han, Y. Guo, and C. K. Lim, "Applications of Moiré and microscopic Moiré interferometry to electronic packaging product development," in *Proc. 4th Annu. IEEE Dual-Use Technol. Appl. Conf.*, Rome, NY, May 1994.

[12] ——, "Applications of interferometric techniques to verification of numerical model for microelectronics packaging design," *Electr. Electron. Packag., Adv. Electron. Packag.*, vol. 10, no. 2, pp. 1187–1194, 1994.

[13] Y. Guo and C. G. Woychik, "Thermal strain measurements of solder joints in second level interconnections using Moiré interferometry," *ASME J. Electron. Packag.*, vol. 114, pp. 88–92, 1992.

[14] B. T. Han, "Higher sensitivity Moiré interferometry for micromechanics studies," *Opt. Eng.*, vol. 31, no. 7, pp. 1517–1526, 1992.

[15] Y. Guo, C. K. Lim, W. T. Chen, and C. G. Woychik, "Solder ball connect (SBC) assemblies under thermal loading: I. Deformation measurement via Moiré interferometry and its interpretation," *IBM J. Res. Develop*, vol. 37, no. 5, pp. 635–648, 1993.

[16] H. C. Choi, Y. Guo, W. LaFontaine, and C. K. Lim, "Solder ball connect (SBC) assemblies under thermal loading: II. Strain analysis via image processing and reliability considerations," *IBM J. Res. Develop*, vol. 37, no. 5, pp. 649–660, 1993.

[17] B. T. Han, "Recent advancements of Moiré and microscopic Moiré interferometry for thermal deformation analyzes of microelectronics devices," *Exp. Mech.*, vol. 38, no. 4, pp. 278–288, 1998.

[18] B. T. Han and Y. Guo, "Determination of an effective coefficient of thermal expansion of elecctronic packaging components: A whole-field approach," *IEEE Trans. Comp., Packag., Manufact. Technol. A*, vol. 19, pp. 240–247, June 1996.

[19] H. Juso, Y. Yamaji, T. Kimura, K. Fujita, and M. Kada, "Board level reliability of CSP," in *Proc. 48th Electron. Comp. Technol. Conf.*, 1998, pp. 525–531.

[20] L. Leicht and A. Skipor, "Mechanical cycling fatigue of PBGA package interconnects," in *Proc. 31st Int. Microelectron. Packag. Soc. Conf.*, San Diego, CA, Nov. 2–4, 1998, pp. 802–807.

[21] U. Perara, "Evaluation of reliability of micro-BGA solder joints through twisting and bending," in *Proc. 30th Int. Symp. Microelectron.*, Philadelphia, PA, Oct. 14–16, 1997, pp. 402–407.

[22] J. Wang, M. Lu, D. Zou, and S. Liu, "Investigation of interfacial fracture behavior of a flip-chip package under a constant concentrated load," *IEEE Trans. Adv. Packag.*, vol. 21, pp. 79–86, Feb. 1998.

[23] D. Post, B. T. Han, and P. G. Ifju, *High Sensitivity Moiré: Experimental Analysis for Mechanics and Materials*. New York: Springer-Verlag, 1994.

[24] Y. Guo and L. Li, "Hybrid method for local strain determinations in PBGA solder joints," in *Numerical/Experimental Mechanics for Electronics Packaging*. Bethel, CT: Soc. Exper. Mech., Inc., 1997, pp. 22–30.

[25] A. Mawer, "Plastic ball grid array (PBGA)," . Phoenix, AZ: Motorola Semiconductor Technical Data AN1231, 1996.
[26] E. Brown and N. R. Sottos, "Thermoelastic properties of plain weave composites for multilayer circuit board applications," TAM. Rep. 878, UILU-ENG-98-6004, 1997.

Eugene A. Stout received the B.S. degree in mechanical engineering from Rensselaer Polytechnic Institute, Troy, NY, in 1994 and the M.S. degree in theoretical and applied mechanics from the University of Illinois at Urbana-Champaign in 1997.

He is a Senior Mechanical Engineer in the Advanced Manufacturing Systems Technology Group, Personal Communications Sector, Motorola, Libertyville, IL.

Nancy Sottos received the Ph.D. degree in mechanical engineering from the University of Delaware, Newark.

She joined the Department of Theoretical and Applied Mechanics, University of Illinois at Urbana-Champaign, in 1991 and is currently an Associate Professor. She worked as a Research Fellow in the Center for Composite Materials, University of Delaware. She has also held visiting research positions at Imperial College, London, U.K., Bell Communications Research, and at the Naval Air Development Center. Her research areas include the mechanics of composite materials, smart materials, and electronic materials.

Andrew Skipor received the Ph.D. degree in engineering mechanics from the University of Illinois, Chicago, supported in part by the Motorola Distinguished Scholar Program.

He is a Principal Staff Engineer with the Design Reliability Group, Motorola Labs, Motorola Advanced Technology Center, Schaumburg, IL. He has been with Motorola over 16 years. His interests include development of methods to evaluate package reliability, numerical simulation, experimental methods such as Moiré interferometry, nonlinear solder mechanics, fatigue, and PCB/HDI mechanics. He has five patents and numerous internal and external publications.

Dr. Skipor received an engineering award and is the Chairman of the Motorola-IEEE/CPMT Graduate Student Fellowship for Research in Electronic Packaging.